Demixing of a three component system with degenerate free energy

Mason Swanson

December 14, 2007

Abstract

We examine a diffusive, incompressible three component mixing system with symmetric, degenerate equilibrium values of the free energy. To the best of our knowledge, this presents the first example of a realization of a phase ordering system with a conserved two component vector order parameter. We present and discuss the dynamics of our system in one, two, and three dimensional systems using the Lattice Boltzmann simulation method. For the two and three dimensional systems, we consider the dynamical scaling exponents for the coarsening of topological defects in the system.

1 Introduction

The theory of phase ordering systems, those that pass from an unordered phase to an ordered multiphase equilibrium, is a field that has received much attention in the recent past [1, 2, 3, 4]. In such systems, we are concerned with the ordering dynamics of these equilibrium phases, which we quantify with the order parameter of the system. The earliest studies in this field considered systems with scalar order parameters, and more recently systems with vector order parameters have also been considered [1, 3]. Even though there has been a good deal of activity in this field, that we know of, there is an absence of any physical manifestations of a system having a conserved vector order parameter. In this paper, we will show that under the appropriate specifications, our three component mixing system fits under this category as a conserved vector system.

In order to better understand our system, we can consider some more familiar examples of phase ordering systems. Here we can consider and illustrate both systems with non-conserved order parameters (NCOP) and those with conserved order parameters (COP), as well as discussing the distinction between systems having scalar order parameters and vector order parameters.

As an example of a NCOP system with a scalar order parameter, let us consider the well known Ising model. Here the order parameter is given by the magnetization of a given site, which can take values of ± 1. Spins are free to change signs based on the orientation of neighboring sites, which want to align spins. Phase ordering occurs in this system when it undergoes a transition to a sub-critical temperature and domains of each spin begin to form. We can extend this example to a NCOP system with a vector order parameter by considering a magnetic system with arbitrary spin orientation. For example, we can consider a planar magnetic system where the orientation of each spin is a vector in the plane. Like the Ising model, these systems have also been heavily studied, and are known as the XY model (for 2 component vectors) and the Heisenberg model (for 3 component vectors). If fact, there have even been applications of NCOP models with vectors with more than 3 components to certain

magnetic systems [5, 6]. NCOP systems with *director* order parameters have also been applied to liquid crystal systems [7]. A director order parameter is symmetric under a half rotation, as opposed to symmetry under a full rotation of the order parameter for the other systems.

As an example of a COP system with a scalar order parameter, we can consider a mixing system similar to our own, except with only two mixing components (A and B). Here, the situation is very similar to the Ising model, but the main difference is that, where a spin of $+1$ can reorient itself to -1 in the Ising model, in the COP case an A particle cannot turn into a B particle. Hence the order parameter, the densities of A and B, is conserved. As we mentioned above, we know of no documented physical realizations of a COP system with a conserved order parameter. For this reason, our system presents a unique opportunity for studying COP systems having vector order parameters.

It is also beneficial to discuss the formal aspects of modeling these systems. In these models, we consider the behavior of an order parameter field $\phi(\mathbf{x}, t)$ subjected to a free energy functional $F(\phi)$. A common form for the free energy is given by

$$F = \int d^d x \left(V(\phi) + \kappa (\nabla \phi)^2 \right). \tag{1}$$

In this free energy, the equilibrium phases correspond to minimum values of the potential term $V(\phi)$, one very common example (for scalar order parameters) is the double well potential

$$V(\phi) = -\frac{1}{2}\phi^2 + \frac{1}{4}\phi^4, \tag{2}$$

which has minimum values for $\phi = \pm 1$. The gradient term in Eq. (1) represents a free energy cost for interface between the phases of the system, the strength of which is dictated by κ.

Interfaces between different phases are important in these systems, because their associated free energy cost becomes important in the phase ordering of the system. For the scaler case (recall examples of the Ising Model for the NCOP case and two component mixing systems for the COP case), these interfaces are domain walls between the two equilibrium phases and represent the simplest case of the general idea of topological defects in phase ordering systems. In order to discuss these defects, we need to define O(n) symmetry; an O(n) system is one with an n component order parameter that is invariant under global rotations of the free energy. Note that the above double well free energy has O(1) symmetry. Defects occur at locations where the free energy has passed through one complete rotation; to avoid singularities at these points, the order parameter must vanish at the core of the defect. For an O(n) system in d spacial dimensions, these defects manifest themselves as $(d - n)$ dimensional structures, since all components of the order parameter must vanish at the defect core. For an O(1) system, domain walls occur at locations where the order parameter changes from -1 to 1, a complete rotation of the free energy; hence, we see that domain walls satisfy this defining characteristic of defects. The following table shows the dimension of defects occurring in different systems.

Physical Dimension	Defect Dimension (scalar)	Defect Dimension (2 component vector)	Defect Dimension (3 component vector)
1	0	none	none
2	1	0	none
3	2	1	0

With these considerations in mind, we are now ready to describe our special three component mixing system. In Section 2, we give a full, formal description of the system as well as discussing and explaining the most important aspects of the model; we also include an introduction to the Lattice Boltzmann method and show how it is applied to our system to handle the simulations. In Section 3, we present and discuss the results of the one, two, and three dimensional simulations of our system. Finally in Section 4, we offer concluding remarks on all of our findings.

2 Formal description of our model

2.1 Description of the system

The system under consideration in this paper is an incompressible three component (A-B-C) mixing system similar to the two component COP system discussed above. The important extension that we make for our system is in our choice of the free energy. Similar to above we consider the free energy

$$F = \int d^d x \left(-\frac{a}{2}\phi^2 + \frac{b}{4}\phi^4 - \sum_{\langle c,c' \rangle} \frac{\kappa_{cc'}}{2} \nabla\rho_c \nabla\rho_{c'} \right), \tag{3}$$

but we now let our order parameter $\phi = \phi(\rho_A, \rho_B, \rho_C)$, where ρ_i is the density of the i^{th} component, be a two component vector, and hence the double well potential now has continuous free energy minimum values symmetric about the origin; these minimum values occur at $\phi = \sqrt{a/b} \equiv \phi_{eq}$. If we now choose our coordinate system so that this circle lies underneath our ternary phase diagram, shown in Figure 1, we obtain a O(2) COP system. The summation over the gradient terms in Eq. (3) still represents the free energy cost for having interfaces in the system, but now associates them between each of the components. In Section 2.3, we discuss why we have formulated the free energy in this way with respect to the gradients in component density as opposed to the order parameter ϕ.

We now need to express our order parameter as we have described it in terms of the density coordinates. To do so, we consider the following transformations. First, we note that since our system is incompressible, we have constant density, so we take $\rho_A + \rho_B + \rho_C = 1$, and therefore, all of the possible compositions for our system are restricted to this plane in ρ-space. To make things more

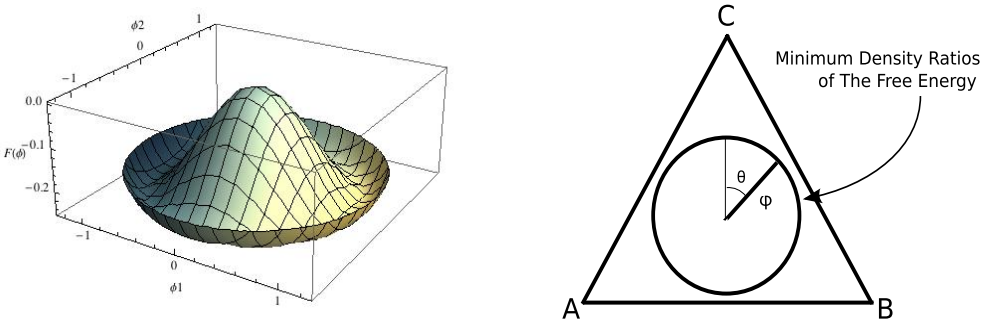

Figure 1: Two component vector case for the double well potential (left). Ternary phase diagram with symmetric, degenerate values of the free energy shown (right).

convenient, we define a new set of coordinates, ϕ_i, so that our new coordinate system sits directly on this plane of constant density. We define this transformation by

$$\begin{pmatrix} \phi_1 \\ \phi_2 \\ \phi_3 \end{pmatrix} = \begin{pmatrix} 1 & 0 & 0 \\ 0 & \alpha/\beta & -\alpha \\ 0 & \alpha & \alpha/\beta \end{pmatrix} \begin{pmatrix} \beta & 0 & -\beta \\ 0 & 1 & 0 \\ \beta & 0 & \beta \end{pmatrix} \begin{pmatrix} \rho'_A \\ \rho'_B \\ \rho'_C \end{pmatrix} = \begin{pmatrix} \beta\left(\rho'_A - \rho'_C\right) \\ -\alpha\beta\left(\rho'_A + \rho'_C\right) + (\alpha/\beta)\rho'_B \\ \alpha\left(\rho'_A + \rho'_B + \rho'_C\right) \end{pmatrix}, \quad (4)$$

where $\beta = \sqrt{1/2}$, $\alpha = \sqrt{1/3}$, and $\rho'_i = \rho_i - 1/3$. Now we have ϕ_1 and ϕ_2 in the plane and ϕ_3 normal to the plane. Note that the origin of our new coordinate system is at the point $\rho_A = \rho_B = \rho_C = 1/3$.

Since we are considering radial symmetry in our system, we use another set of new coordinates ϕ and θ which are shown in Figure 1 and are given by

$$\phi_1 = \phi\cos\theta, \quad (5)$$

$$\phi_2 = \phi\sin\theta. \quad (6)$$

Which are just polar coordinates in the $\rho_A + \rho_B + \rho_C = 1$ plane.

For all of our simulations, we have considered only diffusive dynamics, and used the following equation of motion, a form of the Cahn-Hilliard equation

$$\partial_t \rho_c = \nabla \sum_{c'} m_{cc'} \nabla(\mu_c - \mu_{c'}), \quad (7)$$

where $m_{cc'}$ is a tensor designating the mobility between component c and c', and $\mu_c = \delta F/\delta\rho_c$ is the chemical potential. It can be easily checked that the total density is conserved by this equation. By taking $\kappa_{cc'} = k\delta_{cc'}$, where $\delta_{cc'}$ is the Kronecker delta function and k is constant, we obtain the following form of the chemical potentials

$$\mu_c = \frac{\partial\phi}{\partial\rho_c}\left(-a\phi + b\phi^3\right) + k\nabla^2\rho_c. \quad (8)$$

.

2.2 The Lattice Boltzmann Method

To simulate our systems, we use the Lattice Boltzmann (LB) method. The LB method considers a discretization of the Boltzmann transport equation with BGK approximation. Simply put, the BGK approximation states that the distribution function for a system is changed during particle collisions in such a way that it is brought closer to equilibrium. In the LB method, we consider only a discretized velocity set $\{v_i\}$ related to our lattice spacing, where each velocity has a corresponding distribution function f_i. The discrete version of the Boltzmann equation used in our simulations is

$$f_i(x + v_i, v_i, t + 1) = f_i(x, v_i, t) + \frac{1}{\tau}\left(f_i^0 - f_i(x, v_i, t)\right), \quad (9)$$

where f_i^0 is the distribution function in equilibrium, which we can obtain from the moments of the system. This is only a brief introduction to the LB method, for a more detailed description the reader is referred to [8, 9].

Since we conserve only mass, we can in general take the moments as, for component c

$$\sum_i f_i^{c0} = \sum_i f_i^c = \rho_c \tag{10}$$

$$\sum_i f_i^{c0} v_{i\alpha} = j_{c\alpha} \tag{11}$$

$$\sum_i f_i^{c0} v_{i\alpha} v_{i\beta} = \Pi_{c\alpha\beta}. \tag{12}$$

Where we are using Greek indicies to denote tensors, that is $v_{i\alpha}$ and $j_{c\alpha}$ are vectors, and $\Pi_{c\alpha\beta}$ is a matrix, each corresponding to component c. Both $j_{c\alpha}$ and $\Pi_{c\alpha\beta}$ are arbitrary, and we will see below how choosing them appropriately allows us to apply the LB method for our situation.

Using the above moments and expanding Eq. (9) to second order, we arrive at the Lattice Boltzmann equation of motion given by

$$\partial_t \rho_c + \nabla j_{c\alpha} = (\tau - \frac{1}{2})\nabla(\partial_t j_{c\alpha} + \nabla_\beta \Pi_{c\alpha\beta}), \tag{13}$$

and now we see how choosing $j_{c\alpha}$ and $\Pi_{c\alpha\beta}$ allows us to use the LB method to simulate the model we want; we can do this by choosing these parameters in such a way that Eq. (13) and Eq. (7) match up. For this project, we consider the following choice

$$j_{c\alpha} = 0 \tag{14}$$

$$\Pi_{c\alpha\beta} = \delta_{\alpha\beta}\left(m \sum_{c'} (\mu_c - \mu_{c'})\right), \tag{15}$$

where we've allowed the value of m in Eq. (7) to be constant and equal for all components.

Our only remaining task in implementing the LB method is to calculate the f_i^0 distribution functions using Eqs. (10) - (12). Also, we will adopt the notation DnQm to refer to a simulation in n spacial dimension using a velocity set of m elements. We used a D1Q3, D2Q5, and D3Q7 model for our one, two, and three dimensional simulations respectively. The velocity sets used were: $v_\alpha = \{-v_x, 0, v_x\}$ for 1D, $v_\alpha = \{-v_y, -v_x, 0, v_x, v_y\}$ for 2D, and $v_\alpha = \{-v_z, -v_y, -v_x, 0, v_x, v_y, v_z\}$ for 3D, where v_i is a unit vector in the i direction. By using Eqs. (10) - (12), we obtain the following general form for the equilibrium distribution functions

$$f_{\pm i}^{c0} = \frac{1}{2} m \sum_{c'} (\mu_c - \mu_{c'}) \tag{16}$$

$$f_0^{c0} = \rho_c - nm \sum_{c'} (\mu_c - \mu_{c'}), \tag{17}$$

where n is the spacial dimension.

2.3 Rewriting the free energy

We also considered rewriting the free energy in the following, more natural, form

$$F = \int d^d x \left(V(\phi) + \frac{1}{2} \sum_{\langle \psi, \psi' \rangle} \lambda_{\psi\psi'} \nabla\psi \nabla\psi'\right), \tag{18}$$

where the sum now extends over pairs of our new coordinates ϕ and θ and $\lambda_{\psi\psi'}$ is now a four component tensor. Writing the free energy in this form would allow us to independently control the free energy cost of gradients in the radial and angular direction. When appropriate, we will comment on the benefits of this freedom in Section 3.

Our analysis concluded that the above expressions of the free energy is equivalent to Eq. (3) if we take

$$\lambda_{\psi\psi'} = \sum_c \left(\frac{\partial\psi}{\partial\rho_c}\right)^{-1}\left(\frac{\partial\psi'}{\partial\rho_c}\right)^{-1} = \lambda_{\psi\psi'}(\phi,\theta), \tag{19}$$

where we have used the fact that $\kappa_{cc'} = k\delta_{cc'}$. Having the above expression for the $\lambda_{\psi\psi'}$ tensor, we are in principle done, since all we have to do to get the desired effects would be to multiply these terms by some tensor $M_{\psi\psi'}$ to specify which gradients we want to have a larger effect.

But we need to consider how the chemical potentials change for our new free energy. These terms are given by

$$\mu_c = \frac{\delta F}{\delta\rho_c} = \frac{\partial\phi}{\partial\rho_c}\frac{\delta F}{\delta\phi} + \frac{\partial\theta}{\partial\rho_c}\frac{\delta F}{\delta\theta}. \tag{20}$$

Since our new $\lambda_{\psi\psi'}$ tensor is a function of the coordinates ϕ and θ, as opposed to the original constant tensor $\kappa_{cc'}$, the chemical potentials contain additional terms. Consider, for example, the free energy

$$\tilde{F} = \int d^d x \lambda(\phi)\nabla\phi\nabla\phi. \tag{21}$$

From which, we obtain the chemical potential

$$\tilde{\mu} = -\lambda'(\phi)(\nabla\phi)^2 - 2\lambda(\phi)\nabla^2\phi. \tag{22}$$

For our free energy, we would obtain terms similar to our original chemical potentials plus a set of terms like the $-\lambda'(\phi)(\nabla\phi)^2$ term in the free energy above.

The above analysis completes the formal side of the problem. All we would need to do to implement the above change would be to calculate the derivative terms in Eq. (19), as well as the derivatives of the $\lambda_{\psi\psi'}$ terms. Even so, comparing the complexity of our new free energy formulation with our old one and considering the benefits, we decided to leave the free energy the way it is presented in Eq. (3). It would have been good to gain the added control by changing the free energy, but given the time constraints imposed by this project, we were satisfied to have completed the above analysis and decided that moving on to new tasks would be more worthwhile.

2.4 Simplifications used in the three dimensional implementation

The above analysis gives a complete description of how we modeled our system for the one and two dimensional simulations, as well as a discussion of why we have formulated the free energy the way that we have. In Section 2.3, we saw the problems that arise when trying to rewrite the free energy. Similar to our analysis above, we have considered a slightly modified form of the free energy in order to simplify our calculations in the three dimensional simulations. We do so in an attempt to reduce the heavy computational strain presented by these simulations.

Since we are most interesting in the behavior of the order parameter $\vec{\phi}$ in our simulations, and not in the densities of the individual components, we now consider simulating two components ϕ_1 and ϕ_2

instead of the densities as we previously did. These components are set up such that $\hat{\phi_1}$ and $\hat{\phi_2}$ are orthogonal coordinates in the phase diagram as they were described previously by Eq. (4). We then have

$$\vec{\phi} = \phi_1 \hat{\phi_1} + \phi_2 \hat{\phi_2}. \tag{23}$$

The simplified form of the free energy used in these simulations is

$$F = \int d^d x \left(-\frac{1}{2}\phi^2 + \frac{1}{4}\phi^4 - \frac{1}{2}\nabla\vec{\phi} \cdot \nabla\vec{\phi} \right), \tag{24}$$

similar to the previous definition, but we have now set $a = 1$, $b = 1$ and $\kappa = 1$, which gives us a new equilibrium value of $\phi_{eq} = 1$. We now use a vector form of our equation of motion given by

$$\partial_t \vec{\phi} = \nabla \left(m \nabla \vec{\mu} \right), \tag{25}$$

where the chemical potential is

$$\vec{\mu} = \frac{\delta F}{\delta \vec{\phi}} = -\vec{\phi} + \vec{\phi}^3 - \nabla^2 \vec{\phi}. \tag{26}$$

We can now separate this equation into the two components corresponding to $\hat{\phi_1}$ and $\hat{\phi_2}$, where each component has the form

$$\mu_i = (\phi^2 - 1)\phi_i - \nabla^2 \phi_i. \tag{27}$$

Our equation of motion is now separable into each individual component and we model Eq. (25) by simulating the two component equations. Similar to before, we match our equation of motion to the Lattice Boltzmann equation of motion, Eq. (13), by taking

$$j_{c\alpha} = 0 \tag{28}$$

$$\Pi_{c\alpha\beta} = \mu_c \delta_{\alpha\beta} \tag{29}$$

$$\tau = m + 1/2. \tag{30}$$

In all of our simulations performed using this new formalism, we will consider the case of $m = 1/2$, allowing $\tau = 1$, which simplifies Eq. (9) to

$$f_i(x + v_i, v_i, t + 1) = f_i^0, \tag{31}$$

where we again obtain these equilibrium distribution functions using Eqs. (10) - (12), where we find

$$f_{\pm i}^{c0} = \frac{1}{2}\mu_c \tag{32}$$

$$f_0^{c0} = \phi_c - 3\mu_c. \tag{33}$$

As mentioned above we used a D3Q7 model for our 3D simulations with the velocity set $v_\alpha = \{-v_z, -v_y, -v_x, 0, v_x, v_y, v_z\}$. The new optimized code produced the same dynamics for our system, but ran much faster than the previously developed code, allowing us to run longer and larger 3D simulations. We should in principle be able to do a direct analytic comparison of our two models to see that they are equivalent, but we have not had time to do so.

3 Simulation Results

We have currently conducted research on our system in one, two, and three dimensions. Each of these cases illustrates important aspects of the system, and consequently, we include a discussion of all three below. In each case, the simulations were subject to random initial conditions, where the densities of the three components were all fluctuated about the point of equal mixing. Also, in all of the simulations we have employed periodic boundary conditions. In both the one and two dimensional cases, we considered systems of size 100 lattice sites. We used the following parameters in our 1D simulations $a = 0.05$, $b = 0.4$, $k = 0.05$, and $m = 1$. For our 2D simulations, in order to maintain stability in the simulations, the parameters were all lowered to $a = 0.01$, $b = 0.08$, $k = 0.01$, and $m = 1$. Note that these parameters give an equilibrium value of the order parameter $\phi_{eq} = \sqrt{1/8} \approx 0.3536$ and that the ratio between a, b, and k is the same in the one and two dimensional simulation. The values of a and b are chosen as they are so that they value of ϕ_{eq} lies in the phase diagram, since these simulations were performed with the densities in mind; the values for k and m were chosen to maintain stability. For the three dimensional simulations, the parameters are as specified in Section 2.4.

3.1 One Dimensional Simulation

Before discussing the results of our one dimensional simulations, we can consider the general dynamics of our system. Naturally the system wants to evolve toward equilibrium values of the order parameter, ϕ_{eq}, but it has to do so in such a way that it provides the lowest free energy cost from the interface term. To do this, neighboring sites of the simulation want to have similar density ratios and are consequently driven around the free energy minima circle. This behavior is nicely illustrated in the one dimensional simulations that we performed, as depicted in Figure 2.

Initially, in the one dimensional simulations, the order parameter begins to take equilibrium values, and as it does we begin to see the winding behavior of the system discussed above. At early times, if these winds are too "tight", there is a lower free energy cost associated with flipping the tightly wound lattice sites across the middle of the phase diagram rather than un-winding them. During our analysis, we did not try to derive a threshold tightness for this flipping mechanism even though it would provide an interesting result. Also, in considering this mechanism, it brings up the issue of how we defined our free energy presented in Section 2.3. If we were able to manipulate gradients in the radial and angular directions separately, we would gain some control over the threshold of the flipping in the lattice and could see different dynamics of the system.

Once all of the lattice sites reach ϕ_{eq}, the simulation can only change through changes in θ; we describe this as an "unwinding" process. To describe this process, we need to comment on the fact that, although neighboring lattice sites always lie next to each other around the free energy minima circle, they can do this in two ways: clockwise or anti-clockwise. And when two of these oppositely oriented "winds" meet up, the system begins to gradually un-wind until it consists of one continuous wind around the circle of ϕ_{eq}. This unwinding is illustrated in Figure 3. Once this un-winding process is complete, the only change the system can make is to uniformly distribute itself around its windings. Once it has done this, it comes to equilibrium.

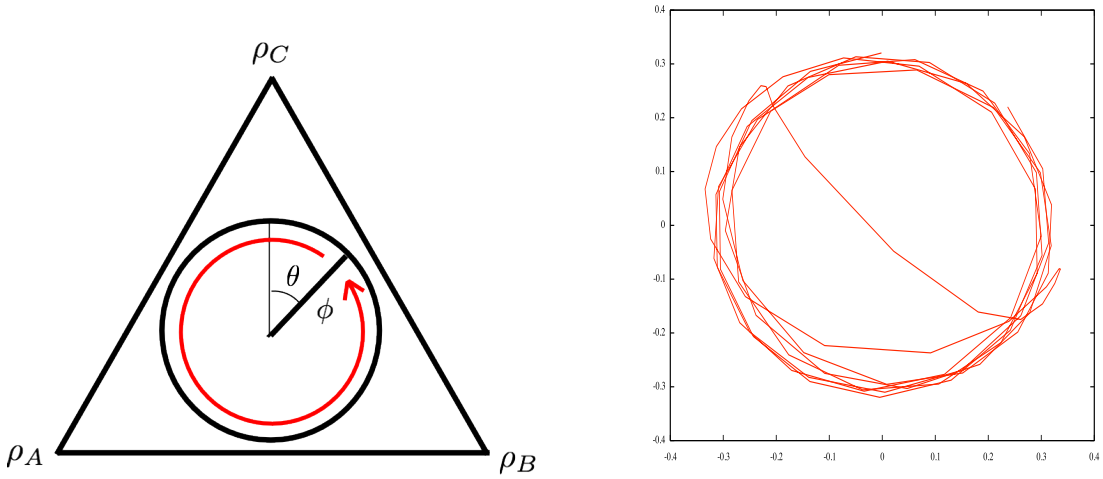

Figure 2: Phase diagram with winding behavior of the simulation (left) and plot of this behavior from a one dimensional simulation (right). In the 1D plot, we also see one of the winds "flipping over," which occurs at early times in the simulation. At later times, all of the dynamics are handled by gradual unwinding of the lattice sites.

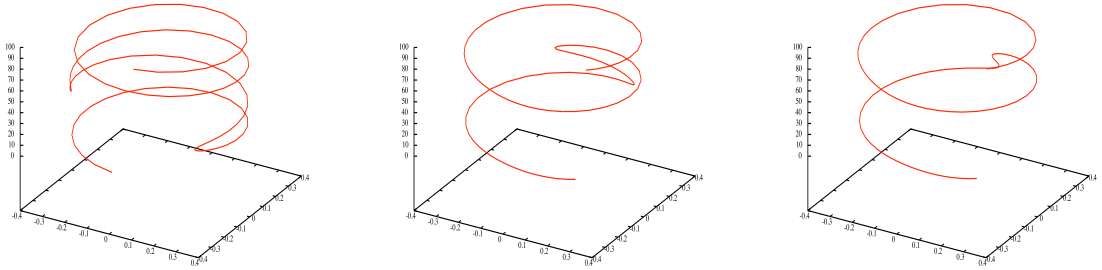

Figure 3: Unwinding of lattice sites in the 1D simulation. The left plot shows the simulation at 80,000, the center at 310,000, and the right at 330,000 iterations. We see in the first plot that at two points on the "helix" of the lattice sites, the path cuts back on itself as a result of opposite orientations of neighboring lattice sites. As the simulation proceeds, the kink in the helix "unwinds" until finally it is completely resolved; which we see the simulation approach in the third plot.

3.2 Two Dimensional Simulations

In the two dimensional simulations, at early times the system phase separates and begins forming regions where $\phi = \phi_{eq}$. Between these regions, during early times, interfaces form with $\phi < \phi_{eq}$ as seen in Figure 4. These interfaces are similar to domains walls we would expect for the scalar order parameter case; they form because the phase separated regions that we initially see are at opposing density ratios in the phase diagram, and so between these regions ϕ must go to zero. As the simulations continues, what we see is that these interfaces themselves phase separate, leaving behind the topological point defects that we expected in the 2D case of our 2-vector model. The appearance of these defects is shown in Figure 4. Once all of the interfaces break up, the dynamics of the system are completely contained in the interaction of the defects.

At this point, we should mention how defects are formed in the simulation. Just as they did in the 1D simulations, due to the cost in interface, neighboring lattice sites want to have similar density ratios, but since they can do so in two dimensions now, it is possible for lattice sites in a closed loop of the lattice to complete a full rotation around the free energy minima circle . In order to maintain continuity, the lattice sites inside of this rotation must allow $\phi \to 0$, it is at these points where the order parameter vanishes that we have defect creation. This is illustrated in Figure 5; we can also see in Figure 5 that defects can have two distinct orientations. Since lattice sites can rotate around the free energy minima circle both clockwise and anti-clockwise, defects can be associated with either of these orientations.

Once the system has phase separated and we see the appearance of defects, the only way for the system to evolve is through defect interaction. Just as a system wants to minimize the amount of domain wall material in the scalar order parameter case, in our vector case the system wants to remove defects whenever possible. This is because there is a free energy cost associated with the defects due to the fact that at the defect core we don't have an equilibrium value of the order parameter. The clockwise/anti-clockwise orientation of defects allows for this interaction and annihilation of defects. On its own, there is no mechanism for a defect to resolve, but when two oppositely oriented defects interact, they can annihilate, and this how the system evolves at later times. The attraction between defects is very low, as they don't provide a very high free energy cost, and the simulation slows down significantly as the defect density becomes low.

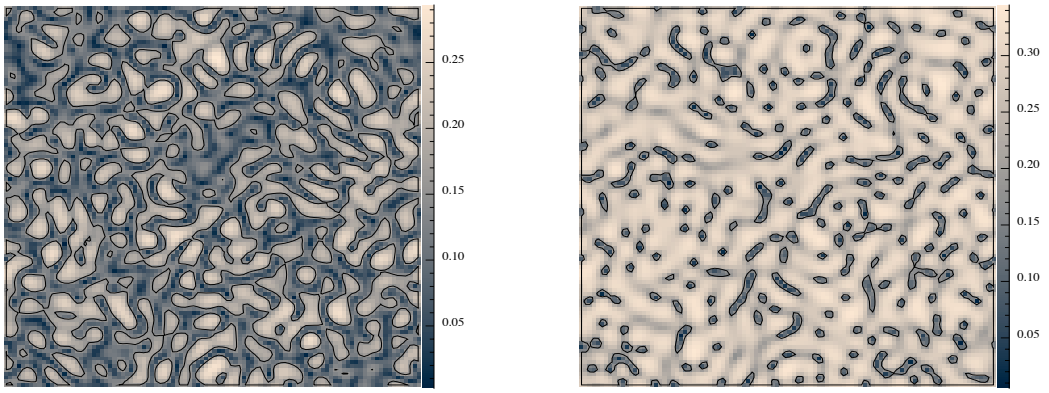

Figure 4: Values of ϕ after 350 (left) and 800 (right) iterations. We see regions of ϕ_{eq} growing in the first plot, and then the appearance of point defects in the second plot.

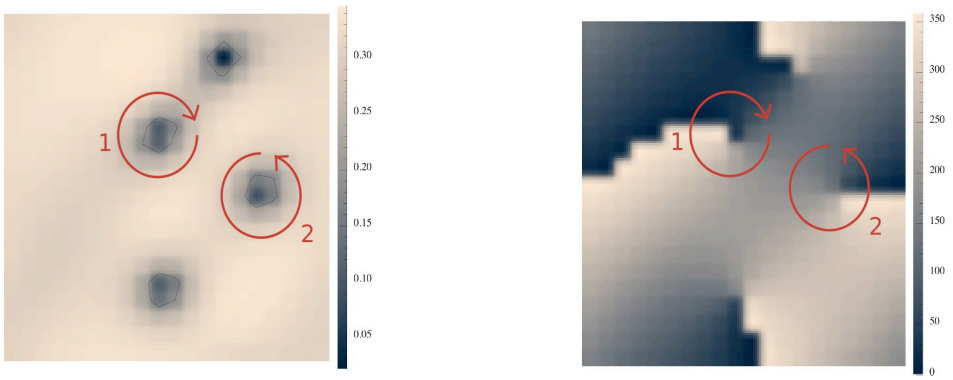

Figure 5: Plot of ϕ (left) and θ (right) showing defect orientation in 2D simulation.

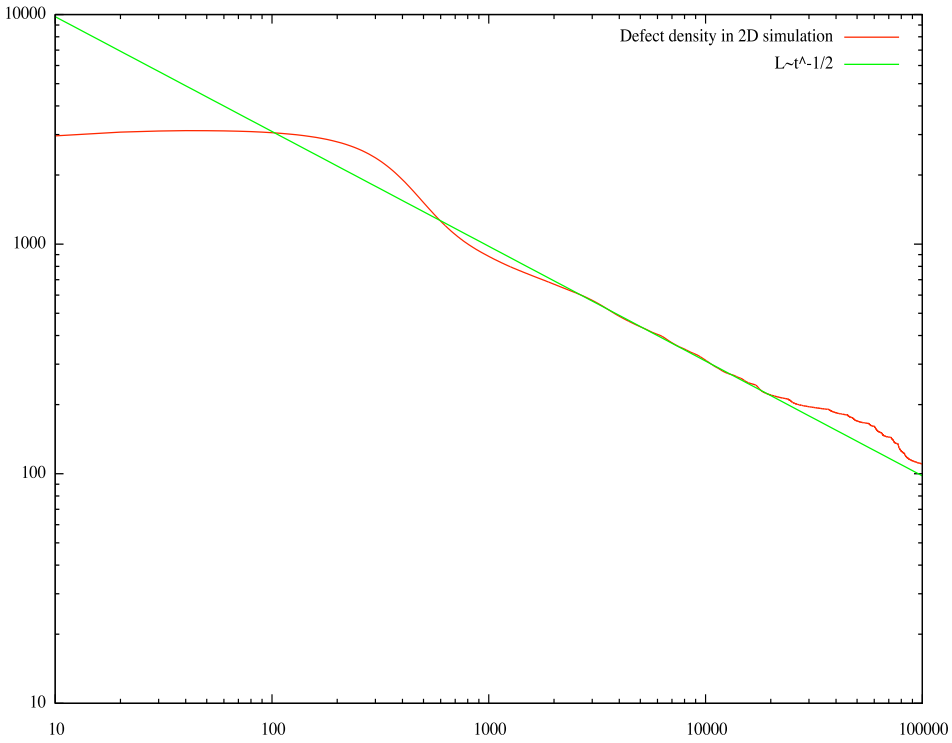

Figure 6: Log-scale plot of $\omega(t)$, the defect density for the first 100,000 iterations of a 2D simulation over a 100x100 lattice. The green line has a slope of $-1/2$. We see that over the first few hundred iterations the system phase separates, and then around 2000 iterations defect iteration drives the system, during this time, we see scaling behavior consistent with $\omega(t) \sim t^{-1/2}$. The deviation at the end of the graph could be caused by the finite size effects of the small lattice or possibly due to some different scaling behavior.

In our two dimensional simulations, we also considered the quantity

$$\omega(t) = \int (\varphi_{eq} - \varphi)\, d^2x, \tag{34}$$

which provided us with an alternative way of studying the evolution of the system. We see that this quantity effectively measures the density of defects in the system and thus describes how close the system is to equilibrium; that is, as the system tends toward equilibrium, $\omega(t) \to 0$. By observing this quantity during the time when the system is driven by defect annihilation, we can see how the density of defects scales with time. Doing so, we found that our results were consistent with

$$\omega(t) \sim t^{-1/2}, \tag{35}$$

which is shown in Figure 6. We see near the end of the plot that there is deviation from this $t^{-1/2}$ behavior. It is unclear whether this is due to the finite size effects of our relatively small simulation (100x100 lattice sites) or if it is due to some different scaling behavior. With this in mind, to obtain a reliable result, we would like to conduct longer simulations on larger lattices.

3.3 Three dimensional simulation

3.3.1 Defect appearance and interaction in the 3D simulations

In the beginning of the simulations, our three dimensional systems evolved very similarly to the two dimensional ones, where at early times we see phase separation cause the system to produce defects and then begin to order through the interaction of these defects. Recall that the dimension of the defects in an O(n) system in d spacial dimensions is given by $d - n$. This is consistent with the point defects seen in two dimensions and predicts line defects in three dimensions, which is exactly what we see in Figure 7. It is easy to see how these line defects are formed by thinking of the point defects in two dimensions as being cross sections of three dimensional defect "tubes." We can also see in Figure 7 how the order parameter completes a rotation around the defect core by observing the continuous color change around each defect.

We can now begin to consider the different ways in which the defects interact in the three dimensional simulations. In contrast to the defects that appeared in our two dimensional simulations, these line defects have much more freedom in their interaction. One major contrast to the 2D defects is that those in 3D can evolve and even annihilate on their own. Solitary defects can minimize their length by reducing their curvature or shrinking, and these solitary defects can shrink in on themselves until they completely disappear.

Even though defects can evolve on their own, the most interesting aspect of their evolution is in how they interact with each other. What happens is that under the right circumstances, two neighboring defects can, and do, combine. This process is illustrated in Figure 8; what happens is that when two defects are near each other, they can change their orientation until adjacent sections of the defects have the same values of θ in the phase diagram, which corresponds to having the same density ratios. When the defects are in this configuration, the two lines can join together without any discontinuity in the continuous gradient of θ. After they have joined, they can pull apart in the opposite direction, again without forming any discontinuities in the θ gradient. Doing this, the two loops join together to form one loop and are then free to coarsen in the way mentioned above, by shrinking and reducing

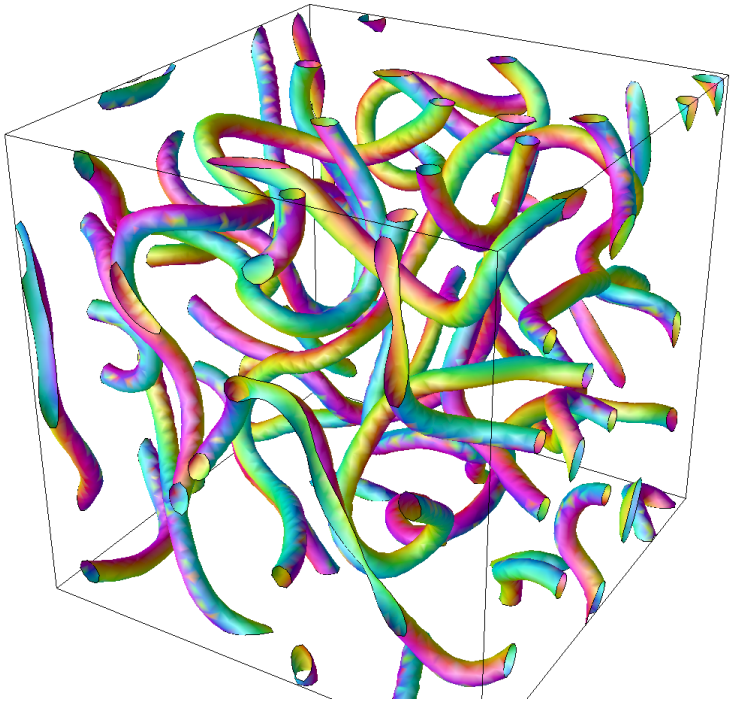

Figure 7: Appearance of defect lines in a 64x64x64 3D simulation. The color of the defect lines signifies the value of θ at that site.

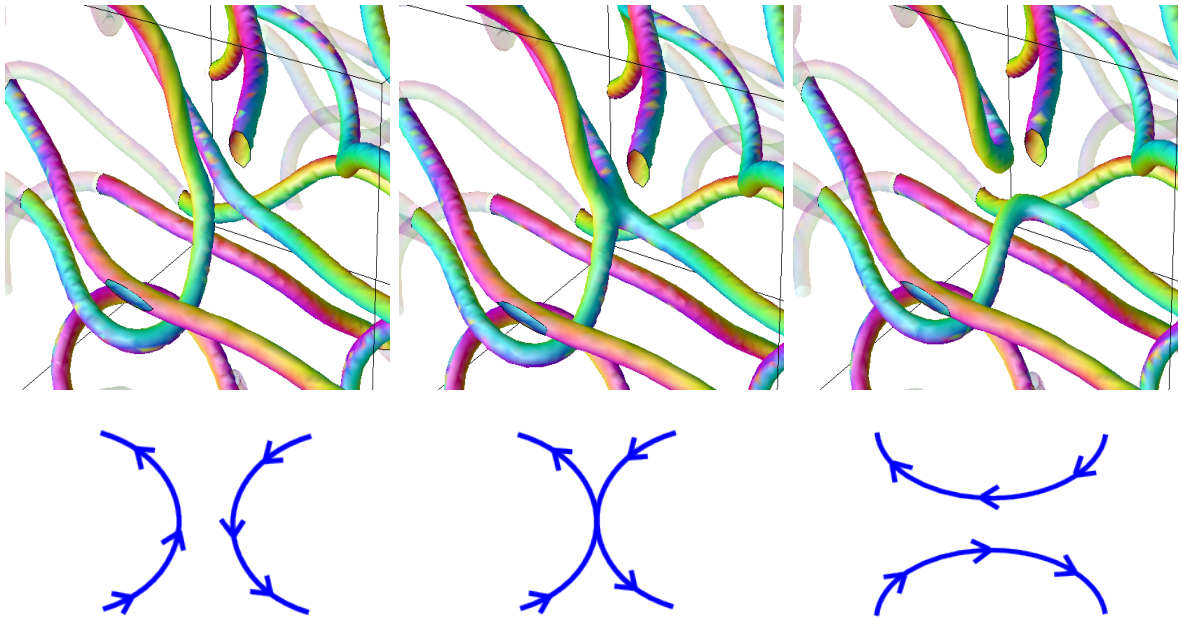

Figure 8: Interaction of neighboring defects; the arrows in the defect representations (bottom row) represent the orientation of the free energy rotation around the defect core. Here we see that the two defects in the middle are attracted to each other if their angles (represented by the color of the defect) match up (left). Once the defects get close enough, they can join up without discontinuities in the order parameter (middle). The two defects then break up again, again with no discontinuity in the order parameter.

their curvature. This process seems to effectively remove a large portion of the defect material in the simulation. Also, we should mention that this process always changes the total number of defects by one. If two different loops join together in this way, the total number of defects is reduced by one, on the other hand, we can also consider the reverse process, where a defect loop interacts with itself to break up into two defects.

3.3.2 Analysis of 3D simulations

To get a better idea of how our system evolves, we considered several different ways to analyze the system. First, we considered the defect density quantity

$$\omega(t) = \int (\varphi_{eq} - \varphi)\, d^3x$$

as we did for the two dimensional case, which gave us interesting results, shown in Figure 9. Since the cross section of the defects is effectively constant, we can consider this quantity as a measure of the total length of defect material in the system. We can see, just as we did in 2D, the phase separation of the system clearly illustrated during early times, but what is interesting in the scaling after the phase separation. In the plot below, we see that some time after phase separation, the defect density begins to scale as

$$\omega(t) \sim t^{-1/2}, \tag{36}$$

as it did in two dimensions. This result is interesting because we have already commented on the different mechanisms available to the 3D simulation for defect annihilation. Given the different ways in which defects can annihilate, we might expect that the scaling is faster in three dimensions, but that is not what we see. Again, we need to comment here on the size of our simulations. The results in Figure 9 are for a 128x128x128 simulation over 15,000 iterations, which is inadequate to provide solid results. In three dimensions, we begin to run into serious computational issues in trying to run simulations of the necessary size to obtain reliable results for measurements such as the defect density. Ideally, we would like to consider a system at least four times the size of this one over time periods of at least one order of magnitude higher than we have done here. To do so, we would have to rethink how we have prepared our code to try to find solutions to these issues.

We were also interested in measuring the actual number of defects in our systems. Being able to measure the number of defects would provide us with an alternative way to measure scaling in the system, and we would also be able to measure how many of our defects were closed curves and how many were strictly periodically continuous (consider an infinite defect line through opposite boundaries of the simulation). To perform this measurement, we used the following method. We went through the system and assigned a field where a site was given a value of -1 if it was part of a defect and -2 otherwise. A routine then investigated the field until it found a value of -1. Once it did, it would assign a value of 0 to that site, and check each of its neighbors to see if they too contained defects. If they did, these sites also were given a value of 0 and their neighbors were checked, and the whole process was repeated until no neighboring sites contained defects. The routine then moved on until it found another site with -1, where is would now mark this site with a 1 and check its neighbors.

This recursive routine was implemented in our simulations, and we ran simple tests by setting up straight line defects for the algorithm to count. The first implementation of the routine counted

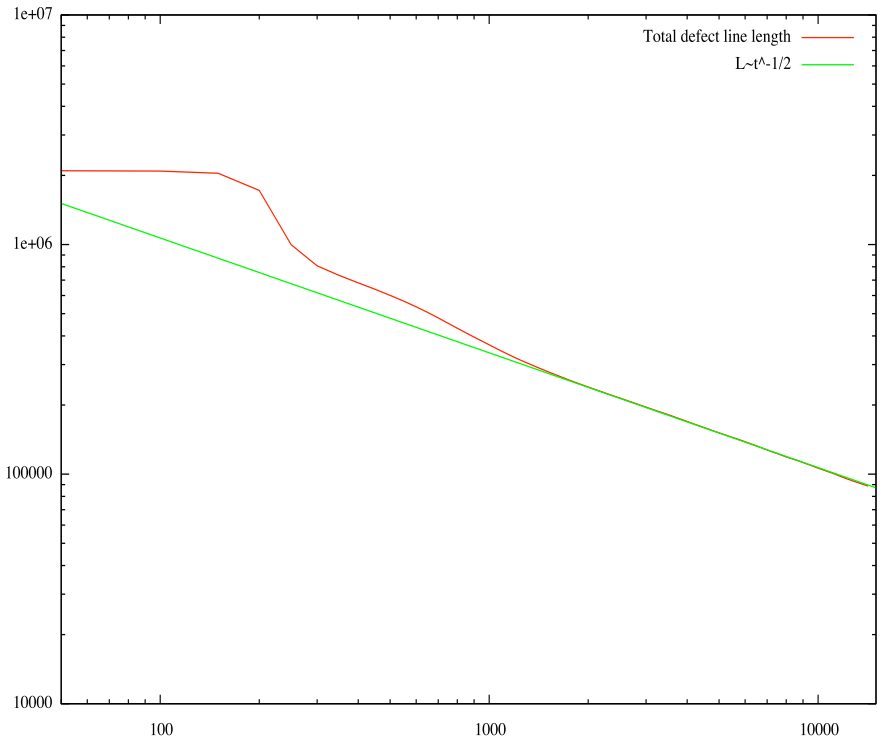

Figure 9: Log scale plot showing scaling of the defect density in a 128x128x128 3D simulation over 15,000 iterations; the green line has slope of -1/2. We can clearly see the phase separation of the system over the first few hundred iterations followed by the defect driven dynamics of the system around 1000 iterations. As we saw in the 2D simulations, during defect interaction the scaling of the defect density is consistent with $\omega(t) \sim t^{-1/2}$.

these defects correctly, but ran into stack overflow issues when we applied it to a larger simulation. We solved this problem by modifying the algorithm to keep it from recursively calling itself too many times, and made sure that the new algorithm passed the simple straight line defect test. There were no computational problems when we applied our new implementation of the algorithm to an actual large simulation, but it still was not counting the defects correctly and unfortunately gave us no reliable results. We have since found a different non-recursive cluster-counting algorithm, outlined in [10], and if we try to repeat these measurements, we will employ this new algorithm rather than debugging our original one.

We also tried to gain insight into the dynamics of our system by setting up simple defect configurations. Providing the simulation with the appropriate initial conditions for defect formation is nontrivial, and we handled it in the following way. We set up single isolated loops by setting the initial radius value throughout the lattice to the equilibrium value ϕ_{eq}; we then used the following configuration for the θ values, using only three different equally spaced values, which we denote by their "color:" red, green, or blue: we colored the top half of the lattice sites green and the bottom blue, then, where we wanted the defect to be arranged, we inserted a cylinder of red. This gives the correct angular configuration (red-green-blue or blue-green-red) for a single defect core to wrap around the cylinder.

We were interested in how quickly a single isolated ring would shrink based on the radius value, but were surprised with what we found. We had expected to find that the isolated ring would shrink quickly, but found that it evolved very slowly and appeared at times almost stable. One of the problems

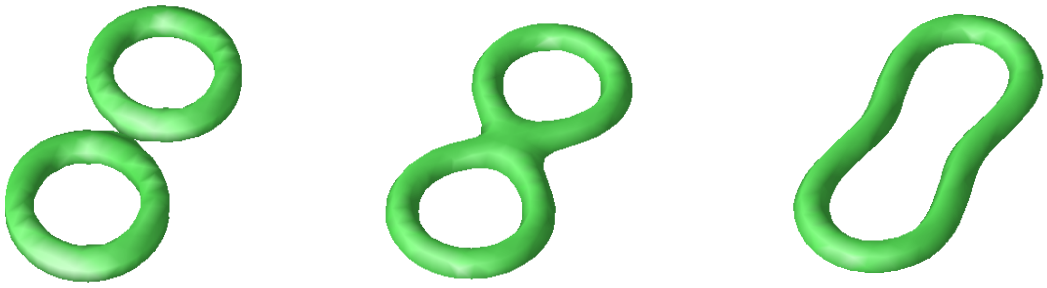

Figure 10: Interaction of two isolated loops for our 50x50x25 simulation. We see that the two loops are initially attracted to each other and join up to form one large isolated loop in the manner described in Section 3.3.1. This loop then begins to shrink away in the normal fashion. The scaling of this system is shown in Figure 11.

with performing these calculations is in determining what it means for the loop to be isolated, since it can also interact with its periodic boundary images. For our simulations, we constructed a loop of radius 5 at the center of a 50x50x25 simulation. The scaling behavior of this loop is given in Figure 11. Here we see how slowly the system scales, and that at times it appears nearly stable. Also, it appears that once the defect radius reaches some critical value, the attraction is strong enough to cause it to shrink quickly. Also, we should note here that in our simulations of these isolated loop systems, we used the 3D version of our original formulation of the system, given in Section 2.1, and not the optimized version, given in Section 2.4. The parameters used were: $a = 0.005$, $b = 0.04$, $k = 0.005$ and $m = 1$; again, these parameters were lowered to keep the simulation stable.

In addition to the single isolated loop system, we also considered a system consisting of two defect loops, again of radius 5, isolated next to each other. Again we considered a 50x50x25 simulation. What happened here is that the two loops were attracted to each other early on in the simulation and joined as described above and seen in Figure 10. If we look at the scaling of this system, shown in Figure 11, what stands out is that the two loop system actually scales more quickly than the one loop system, even though it has twice the initial defect density. This odd characteristic of the scaling in these systems brought up a point that we had not considered. In these systems we should consider the effect of the mean order parameter on the dynamics of the system. When we randomly initialize our system, the mean value of the order parameter is nearly zero, but for these systems it is different. In interpreting these results, we should consider how this affects the dynamics, which we have not done yet.

4 Conclusions

In this paper we have seen that by considering a free energy with continuous degenerate equilibrium values, our three component mixing system is an example of a conserved vector system with O(2) symmetry. This classification of the system is significant since, to our knowledge, there have been no previous systems of this type, even though applications of non-conserved vector and scalar systems and conserved scalar systems have been discussed. These previous results provide context and motivation for researching our system.

We discussed the general behavior of our system and the results of one, two, and three dimensional

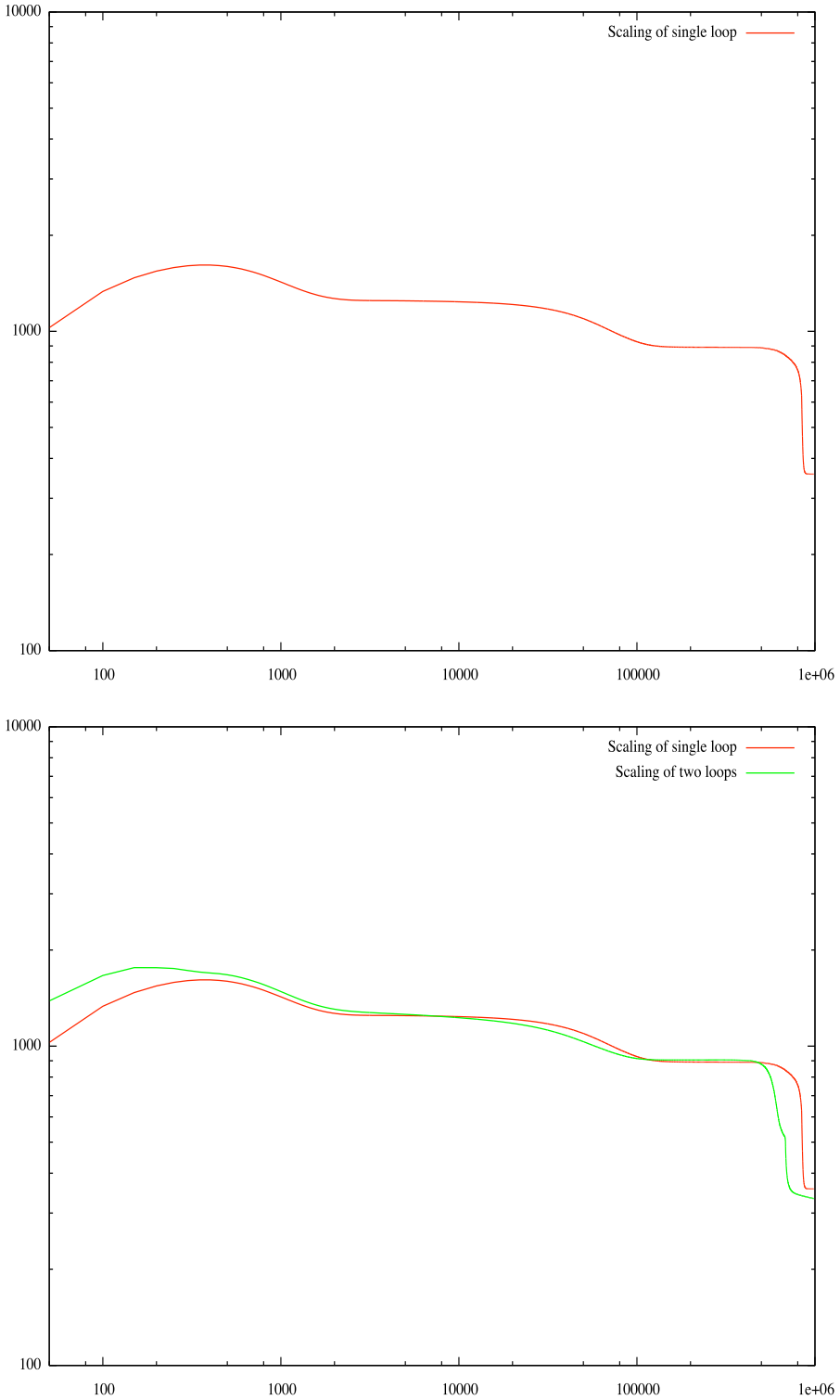

Figure 11: Scaling in isolated loop systems; the plots show the scaling of the defect density, given by Eq. (35), over time, which effectively measures the circumference of the isolated loops since the defects have constant cross-sectional area. The first plot shows the scaling of a single isolated loop of radius 5 lattice sites immersed in a 50x50x25 system. The second plot shows both the scaling of the single loop system and a two loop system where each loop was initialized with a radius of 5 lattice sites and the loops were initially separated by 5 lattice sites. The two loop systems was also part of a 50x50x25 simulation. At the end of the simulations, the systems have resolved their defects. We don't see the density measurement go exactly to zero because the background value of ϕ does not go exactly to the equilibrium value in the simulations.

simulations. Because our system has degenerate equilibrium values around a circle in the phase diagram, we saw that neighboring sites of the simulation were continuously driven around this circle, in order to minimize the difference in density ratios between neighboring sites. This property was illustrated in the one dimensional simulations, where we also saw that the dynamics of the system in 1D were described by a general unwinding of the lattice sites around the equilibrium values of the order parameter. At early times, this unwinding was supplemented by a flipping mechanism for tight winds.

The higher dimensional simulations were highlighted by the appearance of topological defects, analogous to domain walls in the scalar order parameter case. In the 2D simulations, these defects appear as 0 dimensional points. Just as there is an associated free energy cost for domain walls in the scaler case, there is a free energy cost for the defects in our simulation, and this free energy cost drives the phase ordering of the system after phase separation. The dynamics of this defect interaction occur in 2D due to the fact that defects have an associated orientation, either clockwise or anti-clockwise. This orientation allows the defects to interact and annihilate one another.

In our 2D simulations, we also considered the quantity

$$\omega(t) = \int (\varphi_{eq} - \varphi)\, d^2x,$$

which measures the defect density of the system. From this measurement, we found that, for a 100x100 system over 100,000 iterations, our results were consistent with the scaling law

$$\omega(t) \sim t^{-1/2},$$

during times when defect annihilation drove the simulation; although, we also commented on the fact that, in order to obtain more reliable results, we should perform the measurement for larger systems over longer time periods.

In the three dimensional simulations, these topological defects occur as one dimensional defect lines. As they did in two dimensions, the simulations here ordered after phase separation through defect interaction, but in 3D we saw that there were different mechanisms available for defect interaction. One main distinction between the two and three dimensional defect interaction is that in 3D a solitary defect can interact with itself, while in 2D, defects had to annihilate in pairs. Solitary defects were able to evolve by reducing their length and eventually completely shrinking in on themselves. Neighboring defects can interact as well, and we saw that neighboring portions of defect lines can join up, which either reduces the number of defects by one (when two different defects interact) or increases the number of defects by one (one defect interacting with itself).

We performed the same defect density measurement in the 3D simulation that we considered in 2D. And found that our results were again consistent with

$$\omega(t) \sim t^{-1/2},$$

which is somewhat surprising considering the different ways that defects can interact in the three dimensional simulations. The issue of being able to observe large enough systems over long enough time periods is an even bigger problem in 3D, where the computational demand is greater. Our scaling results here are from a 128x128x128 simulation over 15,000 iterations, sizes which are inadequate for solid results. As another way to measure scaling, we wanted to measure the number of defects in our

3D simulations. When we attempted to implement an algorithm to perform this measurement, we first ran into computational issues and then discovered that our algorithm wasn't properly counting the defects, so we unfortunately were unable to get any information our of this effort.

One additional aspect of the three dimensional simulations that we considered was the behavior of isolated loop configurations. We first considered the scaling of a single isolated loop and found that the loop shrunk very slowly. We then considered two neighboring loops. These two loops were initially attracted to each other and joined up to form a single loop which then shank in on itself. The scaling in the two loop system was similar to the single loop system and actually shrank in on itself in a shorter time than the single loop. In our discussion of these isolated loop configurations, we also mentioned the role of the interaction with the defect and its periodic boundary images played in the evolution of the system as well as considering the mean value of the order parameter that comes from our initialization conditions.

Acknowledgments

I would like to foremost thank my senior project advisor, Dr. Alexander Wagner, for his unending advice and motivation. Further, a great thanks is due to Eric Foard for his help in many areas of this project, most notably in optimizing the code and in visualization techniques for the 3D simulations, along with Goetz Kaehler who also provided welcome discussion and support. In addition, I'd like to thank the NDSU Physics Department for providing the resources necessary to complete this project; also I'd like to thank the 2007 Senior Project Review Committee for their advice throughout the completion of this work.

References

[1] A.J. Bray, *Theory of Phase-Ordering Kinetics*, Adv. Phys., **51**, 481 (2002).

[2] G. F. Mazenko and R. A. Wickham, *Vortex Annihilation in the Ordering Kinetics of the O(2) Model*, Phys. Rev. E, **55**, 5113 (1997)

[3] H. Qian and G. F. Mazenko, *Vortex Kinetics of Conserved and Nonconserved O(n) Models*, Phys. Rev. E, **70**, 031104 (2004)

[4] A.J. Bray and K. Humayun, Phys. Rev. Lett., *Scaling and Multiscaling in the Ordering Kinetics of a Conserved Order Parameter*, **68**, 1559 (1992)

[5] D. Murkamel, *Physical Realizations of* $n \geq 4$ *Vector Models*, Phys. Rev. Lett., **34**, 482 (1975)

[6] D. Murkamel and S. Krinsky, *Physical Realization of* $n \geq 4$*-Component Vector Models. I. Derivation of the Landau-Ginzburg-Wilson Hamiltonians*, Phys. Rev. B, **13**, 5065 (1976)

[7] I. Chuang, et. al., *Late-Time Coarsening Dynamics in a Nematic Liquid Crystal*, Phys. Rev. Lett., **66**, 2472 (1991)

[8] Q. Li and A.J. Wagner, *Symmetric Free-energy-based Multicomponent Lattice Boltzmann Method*, Phys. Rev. E, **76**, 036701(2007).

[9] A.J. Wagner, *A Practical Introduction to the Lattice Boltzmann Method*, available online at *www.physics.ndsu.nodak.edu/people/wagner.htm* (2005).

[10] J. Hoshen and R. Kopelman, *Percolation and Cluster Distribution. I. Cluster Multiple Labeling Technique and Critical Concentration Algorithm*, Phys. Rev. B, **14**, 3438(1976)